nanomaterials

MDPI

Article

Epitaxial Growth and Structural Characterizations of $MnBi_2Te_4$ Thin Films in Nanoscale

Shu-Hsuan Su [1], Jen-Te Chang [1], Pei-Yu Chuang [1], Ming-Chieh Tsai [1], Yu-Wei Peng [1], Min Kai Lee [1], Cheng-Maw Cheng [2,3,4,5,*] and Jung-Chung Andrew Huang [1,5,6,*]

1 Department of Physics, National Cheng Kung University, Tainan 701, Taiwan; macg0510@yahoo.com.tw (S.-H.S.); c44051079@gs.ncku.edu.tw (J.-T.C.); chuang.py@nsrrc.org.tw (P.-Y.C.); maggie089621@gmail.com (M.-C.T.); g73582@gmail.com (Y.-W.P.); anion3143@hotmail.com (M.K.L.)
2 National Synchrotron Radiation Research Center, Hsinchu 300, Taiwan
3 Department of Physics, National Sun Yat-sen University, Kaohsiung 80424, Taiwan
4 Graduate Institute of Applied Science and Technology, National Taiwan University of Science and Technology, Taipei 106335, Taiwan
5 Taiwan Consortium of Emergent Crystalline Materials, Ministry of Science and Technology, Taipei 10601, Taiwan
6 Department of Applied Physics, National University of Kaohsiung, Kaohsiung, 811, Taiwan
* Correspondence: makalu@nsrrc.org.tw (C.-M.C.); jcahuang@mail.ncku.edu.tw (J.-C.A.H.)

Abstract: The intrinsic magnetic topological insulator $MnBi_2Te_4$ has attracted much attention due to its special magnetic and topological properties. To date, most reports have focused on bulk or flake samples. For material integration and device applications, the epitaxial growth of $MnBi_2Te_4$ film in nanoscale is more important but challenging. Here, we report the growth of self-regulated $MnBi_2Te_4$ films by the molecular beam epitaxy. By tuning the substrate temperature to the optimal temperature for the growth surface, the stoichiometry of $MnBi_2Te_4$ becomes sensitive to the Mn/Bi flux ratio. Excessive and deficient Mn resulted in the formation of a MnTe and Bi_2Te_3 phase, respectively. The magnetic measurement of the 7 SL $MnBi_2Te_4$ film probed by the superconducting quantum interference device (SQUID) shows that the antiferromagnetic order occurring at the Néel temperature 22 K is accompanied by an anomalous magnetic hysteresis loop along the *c*-axis. The band structure measured by angle-resolved photoemission spectroscopy (ARPES) at 80 K reveals a Dirac-like surface state, which indicates that $MnBi_2Te_4$ has topological insulator properties in the paramagnetic phase. Our work demonstrates the key growth parameters for the design and optimization of the synthesis of nanoscale $MnBi_2Te_4$ films, which are of great significance for fundamental research and device applications involving antiferromagnetic topological insulators.

Keywords: $MnBi_2Te_4$; topological insulators; antiferromagnetic order; molecular beam epitaxy

Citation: Su, S.-H.; Chang, J.-T.; Chuang, P.-Y.; Tsai, M.-C.; Peng, Y.-W.; Lee, M.K.; Cheng, C.-M.; Huang, J.-C.A. Epitaxial Growth and Structural Characterizations of $MnBi_2Te_4$ Thin Films in Nanoscale. *Nanomaterials* **2021**, *11*, 3322. https://doi.org/10.3390/nano11123322

Academic Editor: Sławomir P. Łepkowski

Received: 30 October 2021
Accepted: 2 December 2021
Published: 7 December 2021

1. Introduction

Magnetic topological insulators (TIs) are an attractive platform because their finite magnetic moment provides mass to the massless Dirac fermions, thereby opening an energy gap in an otherwise gapless Dirac state, leading to several emerging topologically driven quantum states [1–3]. Two salient examples are the quantum anomalous Hall (QAH) insulator [4,5] and the axion insulator states [6–8]. These axion insulator states require an atypical magnetic profile; the magnetizations of the top and bottom surfaces of the TI must align oppositely [6–10]. Axion insulators have been observed so far only in atomically tailored TI heterostructures. A natural axion insulator was discovered in layered compound $MnBi_2Te_4$, in which the necessary magnetic profile was achieved through an intrinsic antiferromagnetic coupling of the adjacent atomic layers. Furthermore, upon applying a magnetic field to control the arrangement of the interlayer spins in $MnBi_2Te_4$, the states of QAH insulators and axion insulators become interchanged [11–20]. Axion insulators and Chern insulators have recently been realized in mechanically exfoliated

$MnBi_2Te_4$ flakes [12,21–23], but such flakes are fragile and have small and irregular shapes, thus preventing the large-scale fabrication of devices that utilize the QAH effect. Moreover, the fabrication of $MnBi_2Te_4$ flakes requires heating to a high temperature, which readily causes high-density intrinsic defects. Such defects in $MnBi_2Te_4$ not only cause bulk metallic conductivity, preventing the measurement of the quantum transport of the surface states, but it might also affect magnetic and topological properties [24,25].

In these respects, the molecular beam epitaxy (MBE) method is potentially a promising technique for the synthesis of van der Waals (vdW) materials such as $MnBi_2Te_4$ because the deposition temperature is lower than for flakes grown in thermal equilibrium; the former can decrease the defect concentration [26,27]. Furthermore, the thin-film configuration can provide a suitable platform to realize various artificial $MnBi_2Te_4$ stacking structures, for example, heterostructures and hybrid systems with other materials such as ferromagnets [28–32]. Hence, the MBE growth of high-quality $MnBi_2Te_4$ films is essential for the practical development of devices specifically designed to exploit the remarkable properties of the QAH state and axion insulator state. To date, the MBE growth of $MnBi_2Te_4$ has been pursued by a few groups [31–38]. Despite great effort, the preparation of high-quality $MnBi_2Te_4$ thin films has become a major challenge in this developing field.

In this work, we report the synthesis of $MnBi_2Te_4$ films grown on sapphire substrates with the MBE method. We demonstrate that a self-regulated growth window at the optimal substrate temperature controlled with a Mn/Bi flux ratio emerged through the higher volatility of Te and yielded high-quality $MnBi_2Te_4$ films of a single phase. The MBE growth parameters and structural characterization of the $MnBi_2Te_4$ films were studied with X-ray diffraction (XRD) and Raman spectra. The magnetic properties of $MnBi_2Te_4$ thin films characterized with SQUID indicate that antiferromagnetic order occurring at Néel temperature 22 K was accompanied by an anomalous magnetic hysteresis loop along the *c*-axis. The band structure studied with angle-resolved photoemission spectra revealed a Dirac-like surface state. This work establishes a systematic approach to the epitaxial growth of high-quality $MnBi_2Te_4$ films for future device applications.

2. Experimental Section

The $MnBi_2Te_4$ samples were grown on *c*-plane Al_2O_3 substrates with the molecular beam epitaxy (AdNaNo Corp., model MBE-9, New Taipei, Taiwan) method in an ultra-high vacuum (UHV) chamber equipped with reflection high-energy electron diffraction (RHEED) [39,40]. Highly pure Mn (99.99%), Bi (99.9999%) and Te (99.9999%) were co-evaporated from Knudsen effusion cells. The cell temperature was adjusted precisely before growth to provide the required flux, which was calibrated with the beam flux monitor. Before loading Al_2O_3 substrates into the growth chamber, the Al_2O_3 substrates were ultrasonically cleaned in acetone, isopropyl alcohol and deionized water for 10 min, respectively, and then blown by pure N_2 to the surface before being loaded into the growth chamber. To remove possible contaminants on the surface, the Al_2O_3 substrates were heated to 1000 °C and kept for 1 h before the growth of the $MnBi_2Te_4$ films. During the growth, the Te flux was supplied in excess to overcome the high volatility and to decrease the formation of Te defects. The composition of the films was controlled by the Mn/Bi flux ratio. The flux ratio of Mn/Bi is calibrated with the beam flux monitor (BFM), which is an ion gauge that can measure the equivalent pressure of the molecular beam. To facilitate the epitaxial growth of $MnBi_2Te_4$, a Bi_2Te_3 buffer layer (1 quintuple layer, QL) was first grown on the Al_2O_3 substrate at a substrate temperature of 370 °C. The Bi_2Te_3 layer was further annealed to the desired growth temperatures under Te-rich conditions; the $MnBi_2Te_4$ films were then deposited on the buffer layers. The nominal growth rate of the Bi_2Te_3 and $MnBi_2Te_4$ films were QL/7 min and SL/4 min, respectively. The samples used for SQUID, angle-resolved photoemission spectra (ARPES) and a scanning tunneling microscope (STM) were covered in situ with amorphous Te capping layers (1~2 nm) in an MBE system to avoid surface oxidation. The crystalline condition of the grown thin film was monitored in situ with RHEED. X-ray diffraction (XRD), a high-resolution transmission electron mi-

croscope (HRTEM) and Raman spectra provided structural characterization. The Raman spectra were recorded on a micro-Raman spectrometer with an excitation wavelength of 532 nm. The elemental composition of the samples was calibrated with a transmission electron microscope energy-dispersive system (TEM-EDS) (see Supplementary Materials). The surface morphology was characterized with an atomic force microscope (AFM). The magnetic properties as a function of temperature from 5 to 300 K were measured with a SQUID magnetometer (Quantum Design MPMS SQUID VSM system). An external magnetic field was applied to the surface of the epitaxial layer in either an in-plane or out-of-plane direction. The diamagnetic contribution of the Al_2O_3 substrate was determined from the slope of the magnetization M (H) recorded at large magnetic fields and at 300 K, well above the Néel temperature of $MnBi_2Te_4$; the derived substrate contribution was then subtracted from the raw data recorded at a lower temperature. The ARPES experiment was performed at beamline 21B1 of Taiwan Light Source in the National Synchrotron Radiation Research Center (NSRRC). Before the ARPES measurement, the Te-covered $MnBi_2Te_4$ film was annealed at 180 °C for about 1 h to remove the capping Te layer. ARPES were recorded in a UHV chamber equipped with a hemispherical analyzer (VG Scienta R4000, Uppsala, Sweden) [41]. All spectra were recorded at 80 K under base pressure 8.3×10^{-11} torr and at incident photon energy 24 eV. The angle resolution was about 0.2°; the overall energy resolution was better than 12 meV.

3. Results and Discussion

3.1. Structural Characterizations

To understand the structural evolution of a $MnBi_2Te_4$ film as a function of the Mn/Bi flux ratio (φ_r) and the growth temperature (T_G), we performed X-ray diffraction (XRD) studies on samples in two series. Figure 1a shows the θ–2θ scans for which φ_r was tuned from 0.09 to 1; T_G was fixed at 410 °C. All $MnBi_2Te_4$ films were *c*-axis (0001)-oriented, which was confirmed with a series of signals that closely match the (003n) signals of bulk $MnBi_2Te_4$ [15,42]. Additional signals were observed at about 2θ = 27° and 55°, which are consistent with the formation of a MnTe phase [34]. The intensity of the MnTe phase gradually weakened as φ_r decreased from 1 to 0.1. When φ_r decreased to 0.09, the MnTe phase disappeared, leaving only the $MnBi_2Te_4$ phase. It should be noted that with further decreasing φ_r, the XRD spectrum shows diffraction patterns similar to those of Bi_2Te_3, except that the diffraction peaks are broader than those of Bi_2Te_3. This suggests that at a lower Mn/Bi ratio, Mn atoms mainly act as dopants without significantly changing the crystalline structure of Bi_2Te_3. The trends are consistent with the previous reports [33]. Moreover, compared with the previous study [34], the quartz crystal microbalance (QCM) was used to calibrate the φ_r, which is different from the calibration by BFM in our study. The calibration with the QCM is to measure the frequency response of solid material deposited on the QCM. This φ_r is often linearly related to the ratio of solid materials deposited on the substrate. The calibration method we used is to measure the partial pressure of the molecular beam (Mn, Bi, Te) in the gas phase, and this partial pressure ratio is often not so linear with the ratio of the solid materials deposited on the substrate. This is because the reaction (e.g., sorption and desorption) of gas-phase materials on the substrate can be quite complicated. Therefore, the difference in φ_r between our work and the previous result is likely due to the different calibration methods adopted in the two systems. Figure 1b shows the XRD results for which T_G varied from 310 to 440 °C; the flux ratio was fixed at φ_r = 0.09. For films grown at temperatures 310~340 °C, the intensities of the resolved signals were too weak, but these signals were well distinguished from those of Bi_2Te_3. With T_G increased to 380~410 °C, these signals became well resolved; the intensities increased, which clearly showed the (003n) signals of $MnBi_2Te_4$ [15,34,36,42] with no impurity phase. However, when T_G increased to 440 °C, volatile Bi-Te was desorbed and additional MnTe signals emerged because of the higher growth temperature. The RHEED in situ showed clear strip patterns, indicating a high crystalline quality and a flat surface of the $MnBi_2Te_4$ films, as shown in Figure 1d. Raman spectra were used to investigate

how the change of φ_r affected the lattice vibration and the electron–phonon interaction in the $MnBi_2Te_4$ films, as shown in Figure 1c. The characteristic phonon modes A_{1g}^2, E_g^2 and A_{1g} were identified in the region of a small wavenumber. The Raman spectra of $MnBi_2Te_4$ film have an appreciable blue shift relative to Bi_2Te_3, which is attributed to the stronger in-plane bond of Mn-Te [42]. As φ_r increased from 0.09 to 1, Raman spectra were observed to be red-shifted in these films. The decreasing wavenumber of the vibrational modes (E_g^2 and A_{1g}) is associated with an increase in Mn atoms until the formation of Mn interstitial clusters that might be located in the vdW gaps and connected to the Te atoms of the SL [43]. The optimal growth parameters of the $MnBi_2Te_4$ films occurred at approximately φ_r = 0.09 and T_G = 410 °C. For a thin film prepared under the optimized conditions, the HRTEM was applied to examine the film quality. Figure 1e shows the HRTEM image along the *c*-axis direction, clearly showing the characteristic septuple-layer (SL) structure of the vdW stacking in a $MnBi_2Te_4$ epitaxial film. The film thickness was identified as 7 SL. The atomic structure of each SL is visible in the enlarged image (Figure 1f). As the atomic number of Bi is much greater than that of Te and Mn, the Bi atomic column looks brightest, which is also shown in the inset with the superimposed structural model (see the illustration in Figure 1e). The stoichiometry of the film was estimated using the TEM-EDS as shown in Figure S1 and Table S1 (see Supplementary Materials), which showed that Mn:Bi:Te was 1:2.17:3.99, which is consistent with the chemical formula of compound $MnBi_2Te_4$. These results indicate that, for the epitaxial growth of stoichiometric crystalline $MnBi_2Te_4$ films, the growth temperature and the Mn/Bi flux ratio have narrow windows.

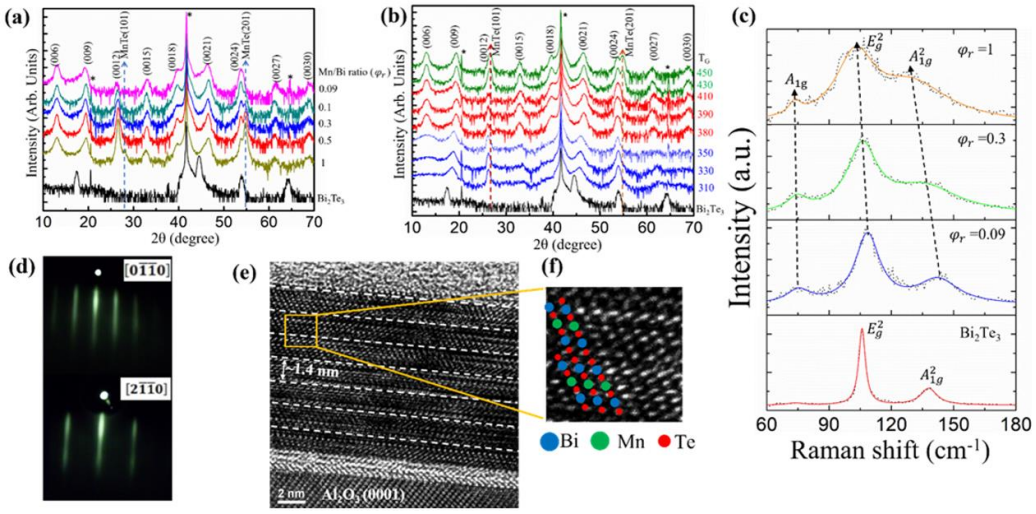

Figure 1. The structural characterizations of epitaxial MnBiTe films under varied growth conditions. The XRD diagrams for (**a**) T_G fixed at 410 °C with varied φ_r and (**b**) φ_r fixed at 0.09 under varied T_G (indicated on the right-hand axis). As indicated in the figure, the signals are marked as *: *c*-plane Al_2O_3 substrate. The dashed vertical arrows highlight the emergence of the MnTe phase. (**c**) Raman spectra of films for varied φ_r. The dotted lines represent raw data; the solid color lines are fits through the raw data. (**d**) RHEED patterns of films along directions $[0\bar{1}10]$ and $[2\bar{1}10]$, respectively. (**e**) TEM cross-sectional view of the film with φ_r = 0.09 and T_G = 410 °C. (**f**) Enlarged TEM image and schematic structure of $MnBi_2Te_4$ are superimposed: blue-Bi, green-Mn, red-Te.

3.2. Surface Morphology

The surface morphology depended strongly on φ_r and T_G. Figure 2a shows the surface of a Bi_2Te_3 film as grown, indicating flat terraces. The surface was composed of characteristic triangular terraces and steps, reflecting the growth of the hexagonal crystal Bi_2Te_3 along (0001) [44,45]. The individual terraces were preferentially aligned with each other; an occasional rotation of 60° was observed, possibly due to the formation of twin boundaries [44]. For φ_r = 0.09 and T_G = 310 °C, the film surface showed misoriented domains with ambiguous shapes and bright islands, which indicated poor crystalline

quality (Figure 2b). The root mean square (rms) roughness was about 6.54 nm. Because T_G was too low, adatoms had insufficient energy to diffuse and to move to sites of least potential energy; they then formed a polycrystalline film. As T_G increased to 410 °C at φ_r = 0.09, the most noticeable feature was the large and flat undefined morphology, as shown in Figure 2c. A significant reduction in 3D bright structures was observed over a large-scale area; its rms roughness was 0.82 nm, which is much less than that of Figure 2b. The layering step is distinguishable on the enlarged surface shown in Figure 2e. The step height is ~1.4 nm (inset of Figure 2e), which is the same as the height of a single SL of $MnBi_2Te_4$ [25,46]. For φ_r = 0.5 and T_G = 410 °C, the surface showed randomly oriented elongated structures, which might be due to the formation of a Mn-rich phase; its rms roughness was 3.85 nm. The STM result revealed that the hexagonal atomic structure on the surface is consistent with the imaging of the topmost Te layer [46,47]; the in-plane lattice parameter was 4.0 Å, as shown in Figure 2f. These structural features confirmed by the AFM and XRD reveal the high quality of the pure $MnBi_2Te_4$ films grown by the delicate MBE method.

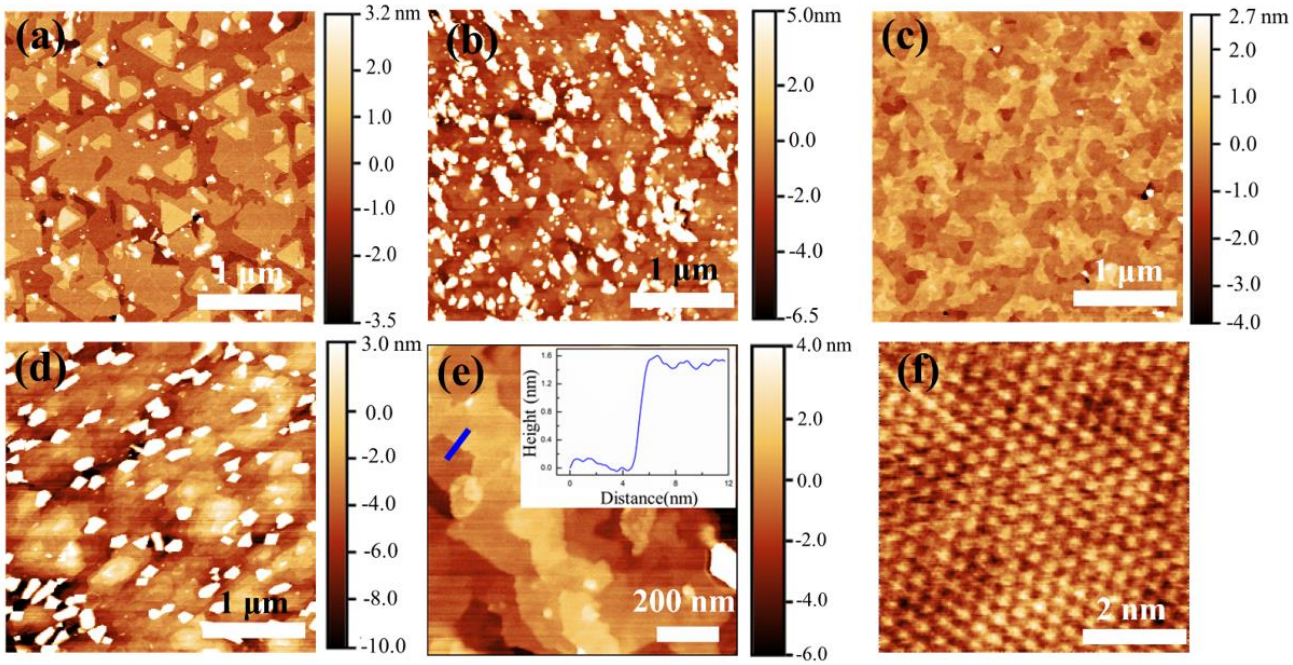

Figure 2. The dependence of film morphology on T_G and φ_r from an AFM: (**a**) Bi_2Te_3 surface (3 μm × 3 μm). (**b**) φ_r = 0.09 and T_G = 310 °C (3 μm × 3 μm); (**c**) φ_r = 0.09 and T_G = 410 °C (3 μm × 3 μm); (**d**) φ_r = 0.5 and T_G = 430 °C (3 μm × 3 μm); (**e**) Magnified AFM image of (**c**); the inset is a height profile along the blue solid line marked in (**e**), showing a step size of 1.4 nm. (**f**) Atom-resolved STM image of (**c**), showing Te-terminated hexagonal atomic structure (size: 6 nm × 6 nm, sample bias: 0.5 V, tunnel current: 0.2 nA).

3.3. Magnetic Properties

In the 2D limit, the odd SL of $MnBi_2Te_4$ exhibit QAH insulators and Chern insulators [14,22,48]. The 7 SL and 11SL $MnBi_2Te_4$ were used to measure the magnetic properties; these properties of a $MnBi_2Te_4$ film were inspected with a SQUID measurement. Figure 3a displays the field-cooled (FC) and zero-field-cooled (ZFC) curves of the 7 SL $MnBi_2Te_4$ film when the magnetic field (~1 T) was along the *c*-axis ($H//c$) and in-plane *ab* ($H//ab$), respectively. The overlapping FC and ZFC curves and λ-shaped feature with an inflection point indicated an A-type antiferromagnetic coupling along the *c*-axis. The Néel temperature (T_N) of the sample was about 22 K, consistent with previous work [15,17,42]. The FC and ZFC curves deviated from each other when the temperature was less than T_N, which implies the emergence of a net ferromagnetic moment. When the field was applied along plane *ab* ($H//ab$), the magnetic moment decreased to one-third, indicating that the $MnBi_2Te_4$ film

had strong magnetic anisotropy. Figure 3b shows the field dependence in plane ($H//ab$) and out of plane ($H//c$) of magnetization curves of a 7 SL $MnBi_2Te_4$ sample. The M–H loop out of plane exhibits a non-linear ferromagnetic shape, whereas the M–H loop in plane is much flatter, indicating a perpendicular magnetic anisotropy with the easy magnetization axis along the c-axis [42,49]. For $H//c$, the M–H curve exhibits an anomalous magnetic hysteresis loop centered at the regime of a small magnetic field, indicating the spin-flip of individual layers and a ferromagnetic feature, which differs from the antiferromagnetic characteristics of $MnBi_2Te_4$ bulk and flakes [42,49,50]. In bulk and exfoliated flakes of $MnBi_2Te_4$, the M–H curves are nominally flat in the regime of a small magnetic field. The residual ferromagnetic response might originate from a possible substrate-induced effect, asymmetric upper and lower surfaces, or uncompensated layers [17,48]. Under magnetic field 3 T, the spin-flip transition occurred as indicated by red arrows in Figure 3b. Similar large-field magnetic behavior was observed in $MnBi_2Te_4$ flakes [42,48–50]. Figure 3c shows the field dependence out of plane of the magnetization curve of a 7 SL $MnBi_2Te_4$ sample in the temperature range from 10 K to 30 K. The anomalous magnetic hysteresis loop dwindled with increasing temperature and disappeared at 30 K, which indicates that a magnetic phase transition from an antiferromagnetic state to a paramagnetic state occurred with increasing temperature, consistent with the observation of M-T curves in Figure 3a. Figure 3d shows the field dependence out of plane of the magnetization curves of a 7 SL $MnBi_2Te_4$ sample for varied φ_r. Compared with the sample with $\varphi_r = 0.09$, for the sample with $\varphi_r = 1$, the magnetic hysteresis loop out of plane vanished because of the in-plane magnetic anisotropy of the MnTe phase [51]. To study the thickness-dependent magnetism, the magnetic properties of $MnBi_2Te_4$ with 7 SL and 11 SL thickness were observed. Figure 3e shows the ZFC and FC curves of 7 SL and 11 SL $MnBi_2Te_4$ films, with the magnetic field (~1 T) along the c-axis ($H//c$). It should be noted that the Néel temperature (T_N) of 11 SL $MnBi_2Te_4$ film slightly increases to 23 K compared to that of 7 SL. Figure 3f shows the out-of-plane M–H loop of 7 SL and 11 SL $MnBi_2Te_4$. The magnetic hysteresis loop centered at the regime of low magnetic fields is persistent in both samples. However, under high magnetic fields, the spin-flip transition of 11 SL is not obvious, which may be due to the tilt or disorder of the antiferromagnetic configuration as the thickness increases.

3.4. Band Structure

The electronic structure of 7 SL $MnBi_2Te_4$ with growth parameters $\varphi_r = 0.09$ and $T_G = 410$ °C was studied with ARPES, which were recorded at 80 K, to which the sample was paramagnetically ordered. Before the ARPES measurements, an XPS experiment after removing the Te capping layer was conducted to confirm the surface condition. Mn 3*p*, Te 4*d* and Bi 5*d* features could be observed clearly from the XPS spectrum, as shown in Figure 4a. Figure 4b,c displays the band-mapping results of a $MnBi_2Te_4$ sample along direction Γ-K and the second derivative of the photoemission intensity, respectively. A Dirac point of $MnBi_2Te_4$ was identified in the band gap and differed from the Dirac point buried in the valence band for Bi_2Te_3 [37,52]. The Fermi level was located above the Dirac point and crossed the bulk conduction band (BCB), indicating that the charge carriers were mainly n-type. The Fermi vector ~0.13 $Å^{-1}$ can be identified from the momentum distribution curve (MDC). The surface carrier concentration estimated from the occupied area of the 2D FS area/the area of surface BZ without counting the spin degeneracy is around ~1.34×10^{13} cm^{-2}, which is higher than that of previous works. [37] This observation indicates that a surface Dirac cone existed in the $MnBi_2Te_4$ film in the paramagnetic state, which is consistent with previous ARPES studies [18,37]. In addition, the band-mapping result exhibits heavily n-doped behavior in this work. A possible reason might be attributed to a higher substrate growth temperature in our work, which could create more Te vacancies or antisite defects. [24,25]

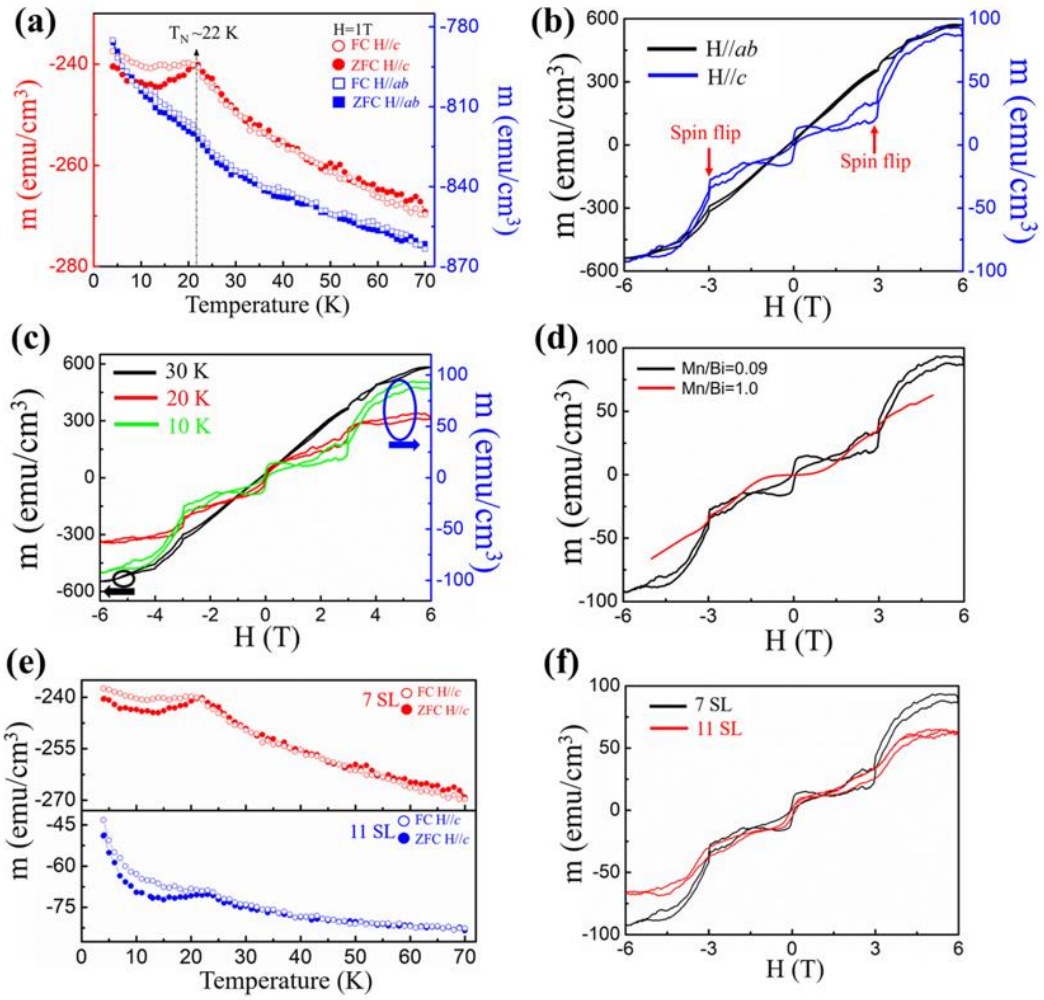

Figure 3. The magnetic properties of a 7 SL $MnBi_2Te_4$ film. (**a**) The temperature dependence of the magnetic moment under ZFC and FC processes with magnetic fields out of plane ($H//c$) and in plane ($H//ab$), respectively. (**b**) The field dependence of the magnetization of a film measured at 10 K with magnetic fields out of plane ($H//c$) and in plane ($H//ab$), respectively. The red arrows indicate the spin-flip transition. (**c**) The field dependence of the magnetization of a film measured at various temperatures with a magnetic field applied out of plane ($H//c$). (**d**) The field dependence of the magnetization of a 7 SL $MnBi_2Te_4$ film at 10 K when a magnetic field out of plane ($H//c$) was applied to samples with φ_r = 0.09 and φ_r = 1.0, respectively. (**e**) The temperature dependence of the magnetic moment under ZFC and FC processes with magnetic fields out of plane ($H//c$) for 7 SL and 11 SL, respectively. (**f**) The field dependence of the magnetization of 7 SL and 11 SL $MnBi_2Te_4$ films at 10 K when a magnetic field out of plane ($H//c$) was applied to samples.

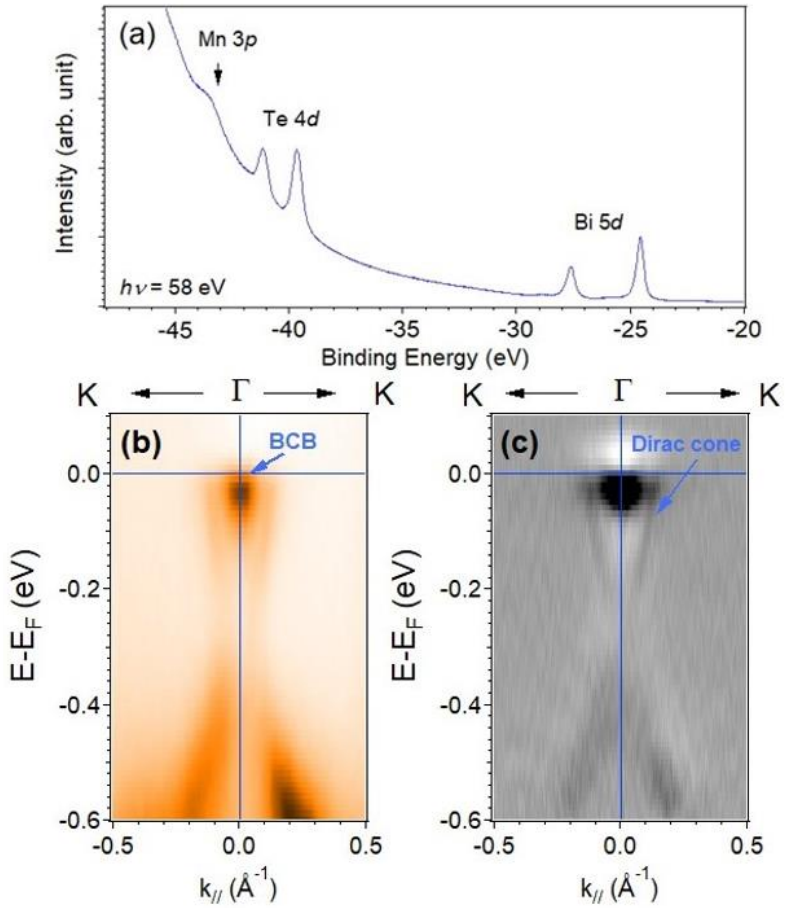

Figure 4. (**a**) The XPS spectrum of $MnBi_2Te_4$ with photon energy 58 eV. (**b**) The band-mapping result of a $MnBi_2Te_4$ sample measured at 80 K along direction Γ-K with photon energy 24 eV. (**c**) The second derivative of (**b**) to enhance the visibility of a Dirac cone.

4. Conclusions

We have presented the synthesis and characterization of $MnBi_2Te_4$ films on a nanometer scale prepared with MBE. In controlling suitable growth conditions, we demonstrated the existence of a self-regulated growth window, resulting in a single phase and the high structural quality of $MnBi_2Te_4$ films confirmed with XRD and Raman spectra. A layered structure of a large area, flat surface and vdW stacking was verified with an AFM and HRTEM. The 7 SL $MnBi_2Te_4$ film showed an antiferromagnetic characteristic with a Néel temperature of 22 K accompanying a low-field anomalous magnetic hysteresis loop along the *c*-axis. The ARPES also confirmed the existence of a Dirac surface state and revealed that the paramagnetic state of $MnBi_2Te_4$ remains a TI. It is worth pointing out that the presence of the MnTe and Bi_2Te_3 impurity phases will greatly reduce or destroy the topological and magnetic properties of $MnBi_2Te_4$. Understanding the synthesis of antiferromagnetic topological insulators in this series with the MBE method opens a huge direction for engineering magnetism and topological states. For example, a $MnBi_2Te_4$ film could be integrated into a heterostructure to enable a functional adjustment. Hence, antiferromagnetic TI/ferromagnetic material heterostructures with exotic quantum phases could be realized [29]. In addition, the antiferromagnetic TI/superconductor heterostructures could provide a platform to explore tunable Majorana bound states [53]. Our work paves the way for future device applications involving antiferromagnetic topological insulators.

Supplementary Materials: The following are available online at https://www.mdpi.com/article/10.3390/nano11123322/s1, Figure S1: TEM-EDX spectrum of $MnBi_2Te_4$ film. Table S1: Atomic ratio of Bi, Mn and Te of the sample.

Author Contributions: M.-C.T. and Y.-W.P. undertook the MBE growth of the samples and the XRD, SQUID, TEM and Raman experiments. S.-H.S. and J.-T.C. performed the STM experiments. P.-Y.C. and C.-M.C. conducted the ARPES experiments. M.K.L. assisted with the SQUID experiments. S.-H.S., C.-M.C. and J.-C.A.H. wrote and revised the manuscript with input from all authors. All authors discussed the results. All authors have read and agreed to the published version of the manuscript.

Funding: We would like to acknowledge the financial support from the Taiwan Ministry of Science and Technology, who financially supported this research under contracts MOST 107-2112-M-213-001-MY3, 110-2112-M-213-016, 110-2124-M-213-002, 110-2124-M-006-008 and 109-2112-M-006-019-MY3.

Data Availability Statement: All data included in this study are available upon request by contact with the corresponding author.

Acknowledgments: The authors gratefully acknowledge the use of XRD 003100, SQUID 000200 and EM 012300 of MOST 110-2731-M-006-001 belonging to the Core Facility Center of National Cheng Kung University.

Conflicts of Interest: The authors declare no conflict of interest.

References

1. Tokura, Y.; Yasuda, K.; Tsukazaki, A. Magnetic topological insulators. *Nat. Rev. Phys.* **2019**, *1*, 126–143. [CrossRef]
2. Yu, R.; Zhang, W.; Zhang, H.-J.; Zhang, S.-C.; Dai, X.; Fang, Z. Quantized Anomalous Hall Effect in Magnetic Topological Insulators. *Science* **2010**, *329*, 61–64. [CrossRef]
3. Chang, C.Z.; Zhang, J.S.; Feng, X.; Shen, J.; Zhang, Z.C.; Guo, M.H.; Li, K.; Ou, Y.B.; Wei, P.; Wang, L.L.; et al. Experimental Observation of the Quantum Anomalous Hall Effect in a Magnetic Topological Insulator. *Science* **2013**, *340*, 167–170. [CrossRef] [PubMed]
4. Chang, C.Z.; Zhao, W.W.; Kim, D.Y.; Zhang, H.J.; Assaf, B.A.; Heiman, D.; Zhang, S.C.; Liu, C.X.; Chan, M.H.W.; Moodera, J.S. High-precision realization of robust quantum anomalous Hall state in a hard ferromagnetic topological insulator. *Nat. Mater.* **2015**, *14*, 473–477. [CrossRef]
5. Checkelsky, J.G.; Yoshimi, R.; Tsukazaki, A.; Takahashi, K.S.; Kozuka, Y.; Falson, J.; Kawasaki, M.; Tokura, Y. Trajectory of the anomalous Hall effect towards the quantized state in a ferromagnetic topological insulator. *Nat. Phys.* **2014**, *10*, 731. [CrossRef]
6. Mogi, M.; Kawamura, M.; Yoshimi, R.; Tsukazaki, A.; Kozuka, Y.; Shirakawa, N.; Takahashi, K.S.; Kawasaki, M.; Tokura, Y. A magnetic heterostructure of topological insulators as a candidate for an axion insulator. *Nat. Mater.* **2017**, *16*, 516–522. [CrossRef] [PubMed]
7. Xiao, D.; Jiang, J.; Shin, J.H.; Wang, W.B.; Wang, F.; Zhao, Y.F.; Liu, C.X.; Wu, W.D.; Chan, M.H.W.; Samarth, N.; et al. Realization of the Axion Insulator State in Quantum Anomalous Hall Sandwich Heterostructures. *Phys. Rev. Lett.* **2018**, *120*, 056801. [CrossRef]
8. Mogi, M.; Kawamura, M.; Tsukazaki, A.; Yoshimi, R.; Takahashi, K.S.; Kawasaki, M.; Tokura, Y. Tailoring tricolor structure of magnetic topological insulator for robust axion insulator. *Sci. Adv.* **2017**, *3*, eaao1669. [CrossRef] [PubMed]
9. Grauer, S.; Fijalkowski, K.; Schreyeck, S.; Winnerlein, M.; Brunner, K.; Thomale, R.; Gould, C.; Molenkamp, L. Scaling of the Quantum Anomalous Hall Effect as an Indicator of Axion Electrodynamics. *Phys. Rev. Lett.* **2017**, *118*, 246801. [CrossRef] [PubMed]
10. Allen, M.; Cui, Y.; Ma, E.Y.; Mogi, M.; Kawamura, M.; Cosma Fulga, I.; Goldhaber-Gordon, D.; Tokura, Y.; Shen, Z.-X. Visualization of an axion insulating state at the transition between 2 chiral quantum anomalous Hall states. *Proc. Natl. Acad. Sci. USA* **2019**, *116*, 14511–14515. [CrossRef]
11. Otrokov, M.M.; Klimovskikh, I.I.; Bentmann, H.; Estyunin, D.; Zeugner, A.; Aliev, Z.S.; Gass, S.; Wolter, A.U.B.; Koroleva, A.V.; Shikin, A.M.; et al. Prediction and observation of an antiferromagnetic topological insulator. *Nature* **2019**, *576*, 416–422. [CrossRef] [PubMed]
12. Liu, C.; Wang, Y.; Li, H.; Wu, Y.; Li, Y.; Li, J.; He, K.; Xu, Y.; Zhang, J.; Wang, Y.; et al. Robust axion insulator and Chern insulator phases in a two-dimensional antiferromagnetic topological insulator. *Nat. Mater.* **2020**, *19*, 522–527. [CrossRef] [PubMed]
13. Li, J.; Li, Y.; Du, S.; Wang, S.; Gu, B.-L.; Zhang, S.-C.; He, K.; Duan, W.; Xu, Y. Intrinsic magnetic topological insulators in van der Waals layered $MnBi_2Te_4$ family materials. *Sci. Adv.* **2019**, *5*, eaaw5685. [CrossRef] [PubMed]
14. Liu, C.; Wang, Y.; Yang, M.; Mao, J.; Li, H.; Li, Y.; Li, J.; Zhu, H.; Wang, J.; Li, L.; et al. Magnetic-field-induced robust zero Hall plateau state in $MnBi_2Te_4$ Chern insulator. *Nat. Comm.* **2021**, *12*, 4647. [CrossRef] [PubMed]
15. Zeugner, A.; Nietschke, F.; Wolter, A.U.B.; Gaß, S.; Vidal, R.C.; Peixoto, T.R.F.; Pohl, D.; Damm, C.; Lubk, A.; Hentrich, R.; et al. Chemical Aspects of the Candidate Antiferromagnetic Topological Insulator $MnBi_2Te_4$. *Chem. Mater.* **2019**, *31*, 2795–2806. [CrossRef]
16. Chen, Y.J.; Xu, L.X.; Li, J.H.; Li, Y.W.; Wang, H.Y.; Zhang, C.F.; Li, H.; Wu, Y.; Liang, A.J.; Chen, C.; et al. Topological Electronic Structure and Its Temperature Evolution in Antiferromagnetic Topological Insulator $MnBi_2Te_4$. *Phys. Rev. X* **2019**, *9*, 041040. [CrossRef]
17. Deng, Y.; Yu, Y.; Shi, M.Z.; Guo, Z.; Xu, Z.; Wang, J.; Chen, X.H.; Zhang, Y. Quantum anomalous Hall effect in intrinsic magnetic topological insulator $MnBi_2Te_4$. *Science* **2020**, *367*, 895–900. [CrossRef]

18. Hao, Y.J.; Liu, P.F.; Feng, Y.; Ma, X.M.; Schwier, E.F.; Arita, M.; Kumar, S.; Hu, C.W.; Lu, R.E.; Zeng, M. Gapless Surface Dirac Cone in Antiferromagnetic Topological Insulator $MnBi_2Te_4$. *Phys. Rev. X* **2019**, *9*, 041038. [CrossRef]
19. He, K. $MnBi_2Te_4$-family intrinsic magnetic topological materials. *npj Quant. Mater.* **2020**, *5*, 90. [CrossRef]
20. Zhao, Y.; Liu, Q. Routes to realize the axion-insulator phase in $MnBi_2Te_4(Bi_2Te_3)$n family. *Appl. Phys. Lett.* **2021**, *119*, 060502. [CrossRef]
21. Ovchinnikov, D.; Huang, X.; Lin, Z.; Fei, Z.; Cai, J.; Song, T.; He, M.; Jiang, Q.; Wang, C.; Li, H. Intertwined Topological and Magnetic Orders in Atomically Thin Chern Insulator $MnBi_2Te_4$. *Nano Lett.* **2021**, *21*, 2544–2550. [CrossRef] [PubMed]
22. Zhang, S.; Wang, R.; Wang, X.P.; Wei, B.Y.; Chen, B.B.; Wang, H.Q.; Shi, G.; Wang, F.; Jia, B.; Ouyang, Y.P.; et al. Experimental observation of the gate-controlled reversal of the anomalous Hall effect in the intrinsic magnetic topological insulator $MnBi_2Te_4$ device. *Nano Lett.* **2020**, *20*, 709–714. [CrossRef] [PubMed]
23. Zhang, D.Q.; Shi, M.J.; Zhu, T.S.; Xing, D.Y.; Zhang, H.J.; Wang, J. Topological Axion States in the Magnetic Insulator $MnBi_2Te_4$ with the Quantized Magnetoelectric Effect. *Phys. Rev. Lett.* **2019**, *122*, 206401. [CrossRef] [PubMed]
24. Du, M.-H.; Yan, J.; Cooper, V.R.; Eisenbach, M. Tuning Fermi Levels in Intrinsic Antiferromagnetic Topological Insulators $MnBi_2Te_4$ and $MnBi_4Te_7$ by Defect Engineering and Chemical Doping. *Adv. Funct. Mater.* **2021**, *31*, 2006516. [CrossRef]
25. Hou, F.; Yao, Q.; Zhou, C.-S.; Ma, X.-M.; Han, M.; Hao, Y.-J.; Wu, X.; Zhang, Y.; Sun, H.; Liu, C.; et al. Te-Vacancy-Induced Surface Collapse and Reconstruction in Antiferromagnetic Topological Insulator $MnBi_2Te_4$. *ACS Nano* **2020**, *14*, 11262–11272. [CrossRef] [PubMed]
26. He, L.; Kou, X.; Wang, K.L. Review of 3D topological insulator thin-film growth by molecular beam epitaxy and potential applications. *Phys. Status Solidi RRL* **2013**, *7*, 50–63. [CrossRef]
27. Chen, X.; Ma, X.C.; He, K.; Jia, J.-F.; Xue, Q.K. Molecular Beam Epitaxial Growth of Topological Insulators. *Adv. Mater.* **2011**, *23*, 1162–1165. [CrossRef] [PubMed]
28. Zhu, W.; Song, C.; Liao, L.; Zhou, Z.; Bai, H.; Zhou, Y.; Pan, F. Quantum anomalous Hall insulator state in ferromagnetically ordered $MnBi_2Te_4/VBi_2Te_4$ heterostructures. *Phys. Rev. B* **2020**, *102*, 085111. [CrossRef]
29. Fu, H.; Liu, C.-X.; Yan, B. Exchange bias and quantum anomalous Hall effect in the $MnBi_2Te_4/CrI_3$ heterostructure. *Sci. Adv.* **2020**, *6*, eaaz0948. [CrossRef]
30. Li, Z.; Li, J.; He, K.; Wan, X.; Duan, W.; Xu, Y. Tunable interlayer magnetism and band topology in van der Waals heterostructures of $MnBi_2Te_4$-family materials. *Phys. Rev. B* **2020**, *102*, 081107. [CrossRef]
31. Fukasawa, T.; Kusaka, S.; Sumida, K.; Hashizume, M.; Ichinokura, S.; Takeda, Y.; Ideta, S.; Tanaka, K.; Shimizu, R.; Hitosugi, T.; et al. Absence of ferromagnetism in $MnBi_2Te_4/Bi_2Te_3$ down to 6 K. *Phys. Rev. B* **2021**, *103*, 205405. [CrossRef]
32. Rienks, E.D.L.; Wimmer, S.; Sanchez-Barriga, J.; Caha, O.; Mandal, P.S.; Ruzicka, J.; Ney, A.; Steiner, H.; Volobuev, V.V.; Groiss, H.; et al. Large magnetic gap at the Dirac point in $Bi_2Te_3/MnBi_2Te_4$ heterostructures. *Nature* **2019**, *576*, 423–428. [CrossRef] [PubMed]
33. Zhu, K.J.; Bai, Y.H.; Hong, X.Y.; Geng, Z.H.; Jiang, Y.Y.; Liu, R.X.; Li, Y.Z.; Shi, M.; Wang, L.L.; Li, W.; et al. Investigating and manipulating the molecular beam epitaxy growth kinetics of intrinsic magnetic topological insulator $MnBi_2Te_4$ with in situ angle-resolved photoemission spectroscopy. *J. Phys. Condens. Matter* **2020**, *32*, 475002. [CrossRef] [PubMed]
34. Lapano, J.; Nuckols, L.; Mazza, A.R.; Pai, Y.Y.; Zhang, J.; Lawrie, B.; Moore, R.G.; Eres, G.; Lee, H.N.; Du, M.H.; et al. Adsorption controlled growth of $MnTe(Bi_2Te_3)$n by molecular beam epitaxy exhibiting stoichiometry-controlled magnetism. *Phys. Rev. Mater.* **2020**, *4*, 111201. [CrossRef]
35. Trang, C.X.; Li, Q.; Yin, Y.; Hwang, J.; Akhgar, G.; Bernardo, I.D.; Grubišić-Čabo, A.; Tadich, A.; Fuhrer, M.S.; Edmonds, M.T.; et al. Crossover from 2D Ferromagnetic Insulator to Wide Band Gap Quantum Anomalous Hall Insulator in Ultrathin $MnBi_2Te_4$. *ACS Nano* **2021**, *15*, 13444–13452. [CrossRef] [PubMed]
36. Kagerer, P.; Fornari, C.I.; Buchberger, S.; Morelhao, S.L.; Vidal, R.C.; Tcakaev, A.; Zabolotnyy, V.; Weschke, E.; Hinkov, V.; Kamp, M.; et al. Molecular beam epitaxy of antiferromagnetic $(MnBi_2Te_4)(Bi_2Te_3)$ thin films on BaF_2 (111). *J. Appl. Phys.* **2020**, *128*, 135303. [CrossRef]
37. Gong, Y.; Guo, J.W.; Li, J.H.; Zhu, K.J.; Liao, M.H.; Liu, X.Z.; Zhang, Q.H.; Gu, L.; Tang, L.; Feng, X.; et al. Experimental Realization of an Intrinsic Magnetic Topological Insulator. *Chin. Phys. Lett.* **2019**, *36*, 076801. [CrossRef]
38. Zhao, Y.-F.; Zhou, L.-J.; Wang, F.; Wang, G.; Song, T.; Ovchinnikov, D.; Yi, H.; Mei, R.; Wang, K.; Chan, M.H.W.; et al. Even-Odd Layer-Dependent Anomalous Hall Effect in Topological Magnet $MnBi_2Te_4$ Thin Films. *Nano Lett.* **2021**, *21*, 7691–7698. [CrossRef] [PubMed]
39. Tung, Y.; Chong, C.W.; Liao, C.W.; Chang, C.H.; Huang, S.Y.; Chuang, P.-Y.; Lee, M.K.; Cheng, C.-M.; Li, Y.C.; Liu, C.P.; et al. Tuning the transport and magnetism in a Cr-Bi_2Se_3 topological insulator by Sb doping. *RSC Adv.* **2017**, *7*, 47789–47795. [CrossRef]
40. Su, S.H.; Chuang, P.-Y.; Lee, J.-C.; Chong, C.-W.; Li, Y.W.; Lin, Z.M.; Chen, Y.-C.; Cheng, C.-M.; Huang, J.C.A. Spin-to-Charge Conversion Manipulated by Fine-Tuning the Fermi Level of Topological Insulator $(Bi_{1-x}Sb_x)_2Te_3$. *ACS Appl. Electron. Mater.* **2021**, *3*, 2988–2994. [CrossRef]
41. Su, S.H.; Chuang, P.-Y.; Chen, H.Y.; Wang, C.-H.; Chen, W.-C.; Tsuei, K.-D.; Lee, C.-K.; Yu, S.-H.; Chou, M.M.-C.; Tu, L.-W.; et al. Topological Proximity-Induced Dirac Fermion in Two-Dimensional Antimonene. *ACS Nano* **2021**, *15*, 15085–15095. [CrossRef]
42. Li, H.; Liu, S.; Liu, C.; Zhang, J.; Xu, Y.; Yu, R.; Wu, Y.; Zhang, Y.; Fan, S. Antiferromagnetic topological insulator $MnBi_2Te_4$: Synthesis and magnetic properties. *Phys. Chem. Chem. Phys.* **2020**, *22*, 556–563. [CrossRef] [PubMed]
43. Silva, A.S.; Guimaraes, E.V.; Cano, N.F.; Silva, R.S. Study of vibrational properties of $Bi_{2-x}Mn_xTe_3$ nanocrystals in host glass: Effect of xMn-concentration. *J. Raman Spectrosc.* **2021**, 1–9. [CrossRef]

44. Harrison, S.E.; Li, S.; Huo, Y.; Zhou, B.; Harris, J.S. Two-step growth of high quality Bi_2Te_3 thin films on Al_2O_3 (0001) by molecular beam epitaxy. *Appl. Phys. Lett.* **2013**, *102*, 171906. [CrossRef]
45. Tung, Y.; Chiang, Y.F.; Chong, C.W.; Deng, Z.X.; Chen, Y.C.; Huang, J.C.A.; Cheng, C.-M.; Pi, T.-W.; Tsuei, K.-D.; Li, Z.; et al. Growth and characterization of molecular beam epitaxy-grown $Bi_2Te_{3-x}Se_x$ topological insulator alloys. *J. Appl. Phys.* **2016**, *119*, 055303. [CrossRef]
46. Liang, Z.; Luo, A.; Shi, M.; Zhang, Q.; Nie, S.; Ying, J.J.; He, J.-F.; Wu, T.; Wang, Z.; Xu, G.; et al. Mapping Dirac fermions in the intrinsic antiferromagnetic topological insulators $(MnBi_2Te_4)(Bi_2Te_3)n$ (n = 0, 1). *Phys. Rev. B* **2020**, *102*, 161115. [CrossRef]
47. Yan, J.Q.; Zhang, Q.; Heitmann, T.; Huang, Z.L.; Chen, K.Y.; Cheng, J.G.; Wu, W.D.; Vaknin, D.; Sales, B.C.; McQueeney, R.J. Crystal growth and magnetic structure of $MnBi_2Te_4$. *Phys. Rev. Mater.* **2019**, *3*, 064202. [CrossRef]
48. Yang, S.; Xu, X.; Zhu, Y.; Niu, R.; Xu, C.; Peng, Y.; Cheng, X.; Jia, X.; Huang, Y.; Xu, X.; et al. Odd-Even Layer-Number Effect and Layer-Dependent Magnetic Phase Diagrams in $MnBi_2Te_4$. *Phys. Rev. X* **2021**, *11*, 011003. [CrossRef]
49. Wu, J.Z.; Liu, F.C.; Sasase, M.; Ienaga, K.; Obata, Y.; Yukawa, R.; Horiba, K.; Kumigashira, H.; Okuma, S.; Inoshita, T.; et al. Natural van der Waals heterostructural single crystals with both magnetic and topological properties. *Sci. Adv.* **2019**, *5*, eaax9989. [CrossRef] [PubMed]
50. Xie, H.; Wang, D.; Cai, Z.; Chen, B.; Guo, J.; Naveed, M.; Zhang, S.; Zhang, M.; Wang, X.; Fei, F.; et al. The mechanism exploration for zero-field ferromagnetism in intrinsic topological insulator $MnBi_2Te_4$ by Bi_2Te_3 intercalations. *Appl. Phys. Lett.* **2020**, *116*, 221902. [CrossRef]
51. Kriegner, D.; Výborný, K.; Olejník, K.; Reichlová, H.; Novák, V.; Marti, X.; Gazquez, J.; Saidl, V.; Němec, P.; Volobuev, V.V. Multiple-stable anisotropic magnetoresistance memory in antiferromagnetic MnTe. *Nat. Comm.* **2016**, *7*, 11623. [CrossRef] [PubMed]
52. Chuang, P.-Y.; Su, S.H.; Chong, C.-W.; Chen, Y.-F.; Chou, Y.-H.; Huang, J.C.A.; Chen, W.-C.; Cheng, C.-M.; Tsuei, K.-D.; Wang, C.-H.; et al. Anti-site defect effect on the electronic structure of a Bi_2Te_3 topological insulator. *RSC Adv.* **2018**, *8*, 423–428. [CrossRef]
53. Hugdal, H.G.; Rex, S.; Nogueira, F.S.; Sudbø, A. Magnon-induced superconductivity in a topological insulator coupled to ferromagnetic and antiferromagnetic insulators. *Phys. Rev. B* **2018**, *97*, 195438. [CrossRef]